PAPER

Check for updates

Aerobic melt-quenching and glass formation in one-dimensional metal–organic hybrids

Shruti Kirti, [a] Patrick Schlachta,[b] Sebastian A. Hallweger, [b] Gregor Kieslich, [b] Christoph Hartmann[c] and Bikash Kumar Shaw [*ab]

Crystalline hybrid organic–inorganic structures from the coordination polymer (CP)/metal–organic framework (MOF) family have recently emerged as materials which liquify upon heating to high temperature and then transform into glass upon cooling to room temperature. This melt-quenching process for this material family generally requires an anaerobic atmosphere to avoid oxidation of organic components at high temperature. Anaerobicity here brings in extra cost and makes the melt-quenching setup robust. Besides, these hybrid liquids often show intriguing thermal behaviour such as exothermic recrystallization (on cooling), cold crystallization (on reheating), *etc.* which again limits the typical melt-quenching process of glass fabrication and processability. Here we turn to hybrid organic–inorganic structures of the one-dimensional (1-D) family and design five 1-D $(PrPh_3P)_2[M(dca)_4]$ ($PrPh_3P$ = propyltriphenylphosphonium; M = Mn, Fe, Co, Ni, Cu; dca = dicyanamide) compounds which overcome the above hurdles and were successfully vitrified upon direct *in situ* melt-quenching on laboratory time scales under aerobic conditions. The combined spectroscopic and X-ray total scattering studies reveal successful structural characterization of these glasses that largely retain the coordination bonding of the crystalline phase and show valuable physical properties such as low liquid fragility (m), large 'glass-crystal network density deficit' $(\Delta\rho/\rho_g)_{network}$, high glass-forming ability (GFA) and polymer-like mechanical hardness (H).

1 Introduction

Liquid and glass formation were recently observed in (A) $[M(dca)_3]$ (ABX$_3$ type, where A is an organic cation, B is a bivalent 3d transition metal, and X is a dicyanamide anion) hybrid organic–inorganic materials.[1] This is the second class of material (apart from recently reported zeolitic imidazolate frameworks, ZIFs, and various two- and three-dimensional network structures) in the CP/MOF family which melts and forms liquids at high temperature and then solidifies to form glasses upon quenching to room temperature.[2–10] These dca-containing network structures offer great potential for developing structure–property relationships by changing the 'A' site cation, or by utilizing different transition metals on the 'B' site.[11] The bidentate end-to-end binding ability of the dca linker make the decoordination–coordination rearrangement feasible during melting. Certainly the 'equivalent resonance' of this anionic structure also plays a crucial role in accelerating this rearrangement process and aids the occurrence of melting at such low temperatures. This is however associated with several

structural changes, *e.g.* ligand decomposition or rearrangement, reduction in metal oxidation states, formation of defect sites, recrystallization and cold-crystallization events, *etc.*[1,12,13] The glass crystallization event is amongst the most critical to optimize for these hybrid network structures.[1,11,13–15] Researchers observed that a high glass-forming ability (GFA), commonly measured by using the T_g/T_m ratio (T_g = glass transition temperature, T_m = melting temperature) and liquid fragility m, resists crystallization of the melt in the supercooled state because of the high viscosity.[16–18] In some cases, the crystallization is completely absent on laboratory time frames, notably for organic glasses such as poly(methyl methacrylate) where it is inhibited due to atacticity (random orientation of functional groups), or by significant crystal-glass density differences *e.g.* in inorganic B_2O_3.[19,20]

In this work, a series of dicyanamide based 1-D A$_2$BX$_4$ (A = propyltriphenylphosphonium; B = =Mn, Fe, Co, Ni, Cu; X = dicyanamide) materials were synthesized and their structure–property relationships explored. All materials show similar configurations and exhibit a 1-D chain like structure (Fig. 1a). The compounds in the series were transformed from solid crystal to viscous liquids, and interestingly, the melting was conducted under aerobic conditions without losing structural integrity. Apart from this, the present series of materials showed a significant difference in the process of glass formation. For

aDepartment of Chemistry, Indian Institute of Technology (BHU), 221 005, India. E-mail: bikashk.chy@iitbhu.ac.in

bDepartment of Chemistry, Technical University of Munich, 85748, Germany

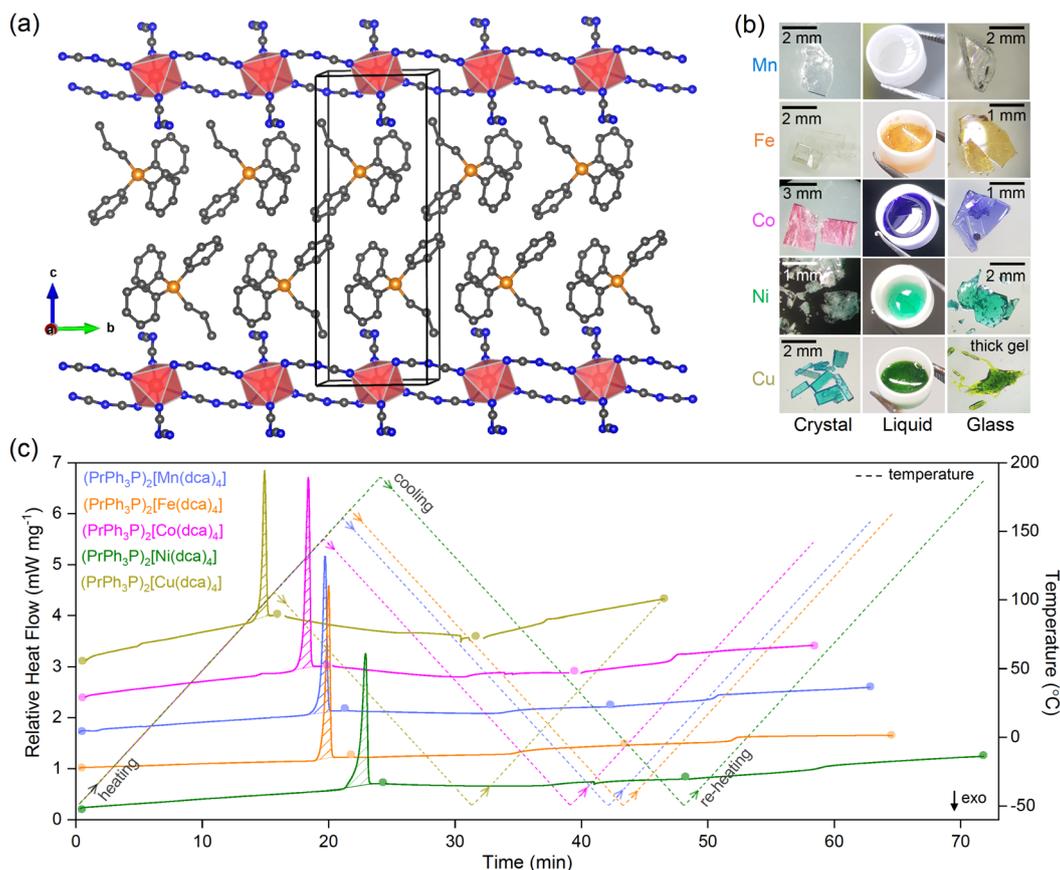*cChair of Metal Forming Casting, Technical University of Munich, 85748, Germany*

Fig. 1 (a) Simplified structure of $(PrPh_3P)_2[Fe(dca)_4]$ at 100 K, showing the 1-D chain configuration of Fe-dca units along the b-axis. Atom colour code: octahedral polyhedra of Fe, red; P, orange; C, grey; N, blue. All H atoms are omitted for clarity. Black lines indicate a unit cell. (b) The optical images of the crystalline solid (left), molten liquid (middle, taken instantly after opening the heating furnace at $T_{m\text{-offset}}$), and quench glass (right). (c) Change in heat flow is shown with respect to both time (x-axis) and temperature (right side y-axis) for the $(PrPh_3P)_2[M(dca)_4]$ crystalline samples (Fig. S8, heat flow vs. temperature). Dotted lines represent the temperature, and circles represent the end of a heating/cooling segment. T_m was determined from the change in the slope at the onset. ΔH_f for the crystalline to liquid transition was extracted from the shaded sigmoidal areas.

example, previously reported liquids of this material family were heated well above T_m (~50 °C beyond $T_{m\text{-offset}}$) before cooling to room temperature.[1] Besides, we have also applied a slower cooling rate to the molten liquids which do not vitrify using the above procedure.[1,11,21] All these processes led to a partial thermal degradation. However, in this work, we are successfully able to apply the typical melt-quenching technique for glass formation.[17] The liquified states of this current 1-D hybrid family were vitrified just after cooling from the $T_{m\text{-offset}}$ at a typical heating-cooling rate of 10 °C min^{-1}. Although CP/MOF based organic–inorganic hybrid glasses have been studied in depth in the last few decades, the problems related to liquid and glass recrystallization and cost-effective and less-robust aerobic melting, remain some of the major issues in the field. The present research aims to explore how tuning A site moieties of dicyanamide based hybrid systems can play a vital role in tuning structural dimensionality which can overcome the above barriers and lead to a new method by which organic−inorganic hybrid glasses could be fabricated via direct in situ open air melt-quenching. In the past decade, several hybrid organic–inorganic materials with varying dimensionality are prone to

liquid/glass formation upon melt-quenching.[7–9] In this regard, the current series of 1-D materials exhibiting typical glass formation under aerobic conditions is fascinating.

2 Results and discussion

2.1 Single-crystal X-ray diffraction study

The block shaped single crystals of the materials were synthesized (procedure given in SI, Fig. 1b, left) and analyzed using a single-crystal X-ray diffractometer (SCXRD) which confirmed the A_2BX_4 framework structure (Fig. S1–S5, Table S1), $(PrPh_3P)_2[Mn(dca)_4]$, $(PrPh_3P)_2[Fe(dca)_4]$, $(PrPh_3P)_2[Co(dca)_4]$, $(PrPh_3P)_2[Ni(dca)_4]$, and $(PrPh_3P)_2[Cu(dca)_4]$. All the compounds crystallize in the $P2_1/n$ space group and exhibit a 1-D structure. The unit cell parameters obtained were then used in a Pawley refinement of powder X-ray diffraction data collected on bulk crystalline powder samples to confirm phase purity in each case (Fig. S6). In $(PrPh_3P)_2[Mn(dca)_4]$, the axial dicyanamide ligands of the 1-D chain exhibit positional disorder (Fig. S1). A strong typical Jahn–Teller distortion (tetragonal elongation) was observed in the $(PrPh_3P)_2[Cu(dca)_4]$ compound (Table 1).

Table 1 Thermo-structural properties of the $(PrPh_3P)_2[M(dca)_4]$ crystals and glasses

$(PrPh_3P)_2[M(dca)_4]$	M–N [Å]	T_d [°C]	T_m [°C]	ΔH_f [kJ mol^{-1}]	ΔS_f [J mol^{-1} K^{-1}]	$a_g(PrPh_3P)_2[M(dca)_4]$			
						T_g [°C]	T_g/T_m [K K^{-1}]	m	H [GPa]
$(PrPh_3P)_2[Mn(dca)_4]$	$(2.17)^a$ 2.25^b	265	142	75	180	36	0.744	36	0.2
$(PrPh_3P)_2[Fe(dca)_4]$	$(2.10)^a$ 2.18^b	270	145	80	192	38	0.744	38	0.2
$(PrPh_3P)_2[Co(dca)_4]$	$(2.07)^a$ 2.15^b	255	128	92	229	32	0.760	43	0.2
$(PrPh_3P)_2[Ni(dca)_4]$	$(2.03)^a$ 2.10^b	265	173	85	191	59	0.744	49	0.6
$(PrPh_3P)_2[Cu(dca)_4]$	$(2.48)^a$ 1.98^b	262	95	61	166	8	0.760	77	Gel

^{a} Represents the axial Mn–N bond distance. ^{b} Represents the average equatorial bond length.

2.2 Thermo-structural analysis

Simultaneous thermogravimetric-heat flow (TG-DSC) analysis of $(PrPh_3P)_2[M(dca)_4]$ crystalline compounds shows temperatures of decomposition (T_d) at 255°–270 °C (Fig. S7, Table 1). We have applied an argon atmosphere for the correct determination of the T_d values to avoid any pre-oxidation process at high temperature near T_d. A broad endotherm was observed for all the compounds in the heat flow behaviour, well before their respective T_d indicating melting. Isolated differential scanning calorimetry (DSC) experiments under aerobic conditions identifies this strong endothermic phase change (Fig. 1c and S8) with an opaque viscous flow (Fig. 1b, middle) attributed to melting. The values of T_m appear at 142°, 145°, 128°, 173°, and 95 °C for M = Mn, Fe, Co, Ni, and Cu analogues, respectively (Fig. 1c, Table 1). The present work reports the lowest T_m [95 °C for $(PrPh_3P)_2[Cu(dca)_4]$] for this dicyanamide based hybrid organic–inorganic material. The enthalpic and entropic changes are expected to correlate with M−N coordination bond strength which (both equatorial and axial) increases from Mn to Cu, in the order Mn–N < Fe–N < Co–N < Ni–N < Cu–N (note that the *axial* Cu–N bond distorts and enlarges to 2.48 Å due to strong Jahn–Teller elongation, Table 1). The corresponding changes in enthalpy (ΔH_f) and entropy (ΔS_f) have been observed to coincide with the *axial* M−N coordination bond strength (Mn–N < Fe–N < Co–N < Ni–N > Cu–N). Weak axial Cu–N bonds in $(PrPh_3P)_2[Cu(dca)_4]$ require less energy for the breaking of M−dca bonds and for the reduction in the average coordination number of M^{2+} during melting. This leads to very small values of ΔH_f and ΔS_f, and hence changes its T_m to this significantly low temperature (95 °C). The $(PrPh_3P)_2[Co(dca)_4]$ material, which follows the above M–N bond strength order, however, does not follow the enthalpic trend and show a comparatively high value of ΔH_f and ΔS_f (Table 1). This thermodynamic effect again explains its irregular and low T_m. This may be due to changes in the geometrical configuration (coordination number) from octahedral to tetrahedral which was evident from the drastic change in colour during melting (faint pink to deep blue, typical for tetrahedral Co^{2+}). It acts as a driving force here and triggers the ΔS_f.

2.3 Formation of melt-quench glass

Subsequent heating–cooling–reheating experiments of all crystalline materials at temperatures ranging from −50 °C to $T_{m\text{-offset}}$ at a rate of 10 °C min^{-1}, reveal endothermic melting during the first heating, glass formation during subsequent cooling, and a clear endothermic 'glass to rubber' phase transition during subsequent reheating, respectively (Fig. 1c and S8). Unlike previous reports, we have witnessed no sign of exothermic recrystallization and cold crystallization for the current network structures during cooling and reheating, respectively.[1,8,10] The *ex situ* PXRD data of the quench DSC solids show glass formation (Fig. S9 and 1b, right). *In situ* glass formation was also studied
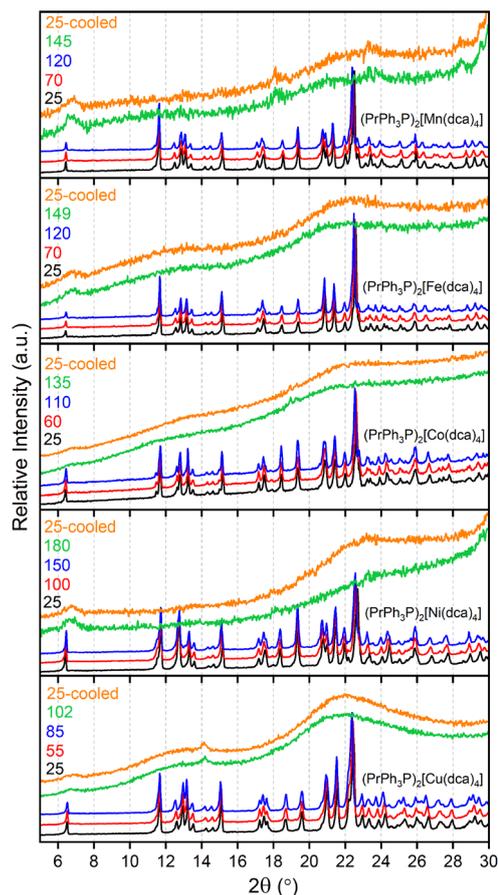

Fig. 2 Variable temperature PXRD patterns of crystalline $(PrPh_3P)_2[M(dca)_4]$ samples. During heating scans, a rate of 10 ($\pm$0.5) °C min^{-1} was applied. To comply with the DSC measurements, the maximum instrumental cooling was applied which provides a rate of 9 ($\pm$1) °C min^{-1}. The absolute temperatures during each 2θ scan were found to be varied by $\pm$1 °C. A small hump at $2\theta = 6.7°$ in every scan (clearly seen in the case of amorphous samples) appeared from the instrument background.

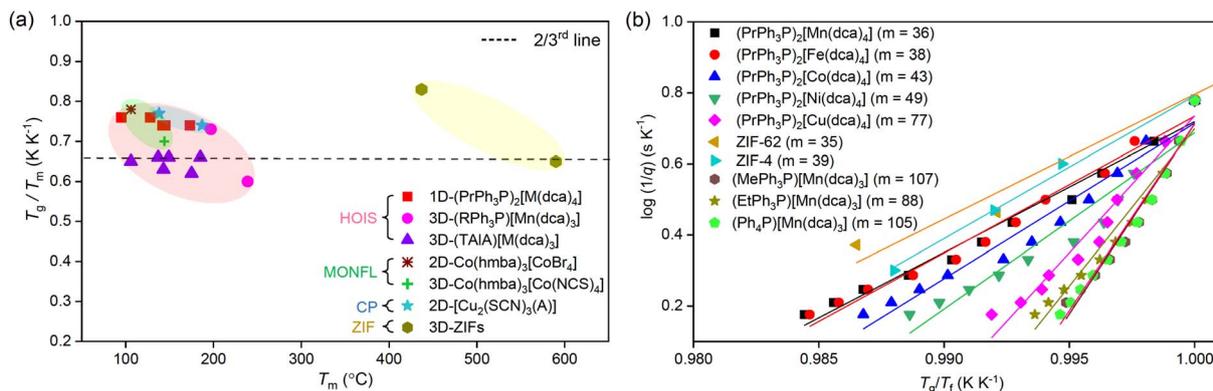**Fig. 3** (a) The comparison of the T_g/T_m ratio (evaluated in Kelvin units) between several low-melting hybrid organic−inorganic structures.[11] The square (red) represents the current $a_g(PrPh_3P)_2[M(dca)_4]$ series. (b) Calorimetric fragility indices (m) of $a_g(PrPh_3P)_2[M(dca)_4]$ were shown with various ZIF and hybrid organic−inorganic systems. The values were evaluated from the dependence of fictive temperature (T_f) on the heating rate (q). The samples were heated from 10−40 °C min^{-1} with 3 °C intervals. The cycles of cooling−reheating of the molten liquid are shown in Fig. S12−S16.

via the variable-temperature powder X-ray diffraction (VT-PXRD) technique (Fig. S10 and S11). PXRD patterns obtained at $T_{m\text{-peak}}$ (peak temperature of the DSC endotherm) show a smooth broad hump with the absence of any Bragg diffraction peak due to melting (Fig. 2). To obtain the diffraction pattern of the quenched solids, the liquids were heated up to their $T_{m\text{-offset}}$ and then cooled to room temperature. PXRD patterns of the quenched solids resemble their molten state with no Bragg diffraction peak and show complete amorphous nature. In line with existing nomenclature of hybrid glasses,[22,23] the present glasses are labelled $a_g(PrPh_3P)_2[M(dca)_4]$ (a_g: amorphous glass).

2.4 Characterization of melt-quench glass

The T_g for $a_g(PrPh_3P)_2[M(dca)_4]$ appears at 36°, 38°, 32°, 59°, and 8 °C for M = Mn, Fe, Co, Ni, and Cu respectively (Fig. 1c or S8). Quenched liquids solidified to form firm glasses at room temperature (Fig. 1b, right). $a_g(PrPh_3P)_2[Cu(dca)_4]$ appears semi-solid (thick gel) at room temperature due to its low T_g. The T_g/T_m ratio shows a deviation from the empirical '2/3rd' law of glass formation with relatively high values, *i.e.* 0.744 (±0.002) for Mn, Fe, and Ni and 0.760 (±0.003) for Co and Cu, respectively (Fig. 3a, Table 1). The values of the kinetic fragility index (m) were evaluated using the DSC technique to detect the glass forming ability (Fig. 3b and S12−S16, Table 1). Low values of m (36, 38, 43, 49, and 77 for Mn-, Fe-, Co-, Ni-, and Cu-analogues) for these hybrid organic−inorganic liquids (except Cu) show similarity to the ZIF-based liquids *e.g.* ZIF-62 ($m = 39$) and also indicate their fragile nature.[24] The present phenylphosphonium based glasses tend to exhibit brittle behaviour contrary to the recently reported similar higher dimensional $a_g(R)[Mn(dca)_3]$ glasses (where R = Ph_4P, $EtPh_3P$, $MePh_3P$) which were ductile in nature ($m = \sim100$).[21]

2.4.1 Elemental and magnetic study. Elemental analysis (C, N, H, and P) shows trivial changes in the elemental compositions upon melt-quenching (Table S2). The respective changes in elemental % from crystals to glasses were <1−2% for C, <1−2% for H, and <2−4% for N. No significant change is observed for P. Furthermore, temperature variation of magnetic

susceptibility was investigated for crystals and glasses to check the formation of any reduced metal centers, M(ɪɪ) → M(0), during melting. The room temperature magnetic moment (μ_{RT} (B.M.) = $2.83\sqrt{\chi_M T}$; χ_M: molar susceptibility) obtained from the variation of the effective magnetic moment ($\mu_{effective}$) with T (Fig. S17a) for all crystalline phases was in good agreement with

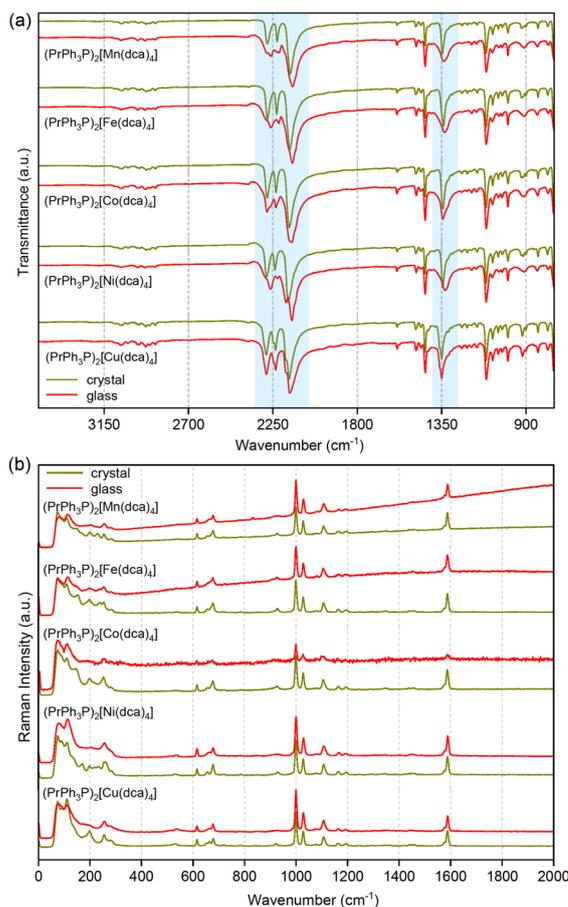**Fig. 4** (a) FT-IR spectra and (b) Raman spectra of $(PrPh_3P)_2[M(dca)_4]$ crystals (dark yellow) and glasses (red).

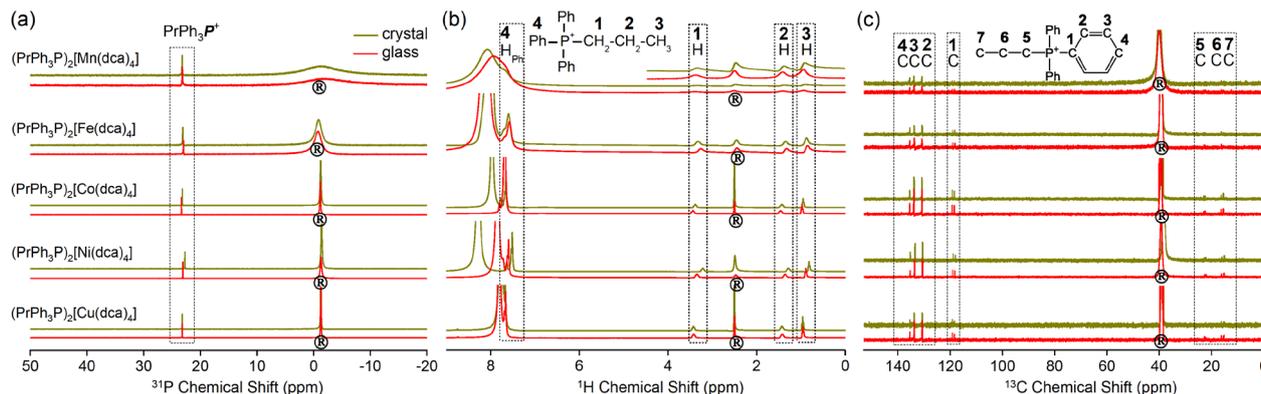**Fig. 5** Liquid phase NMR spectra. (a) ^{31}P NMR, (b) ^{1}H NMR, and (c) ^{13}C NMR spectra of (dark yellow) (PrPh$_3$P)$_2$[M(dca)$_4$] and (red) a_g(PrPh$_3$P)$_2$[M(dca)$_4$]. Circular R symbols in (a) denote the ^{31}P H$_3$PO$_4$ signal near 0.00 ppm, the ^{1}H signal corresponds to the residual protons in DMSO-d_6 near 2.50 ppm in (b), and the signal at 39.50 ppm corresponds to the DMSO-d_6 solvent in (c).

the number of unpaired spins of high spin M(II) species. The decreasing trend of $\mu_{effective}$ at lower temperatures implies the effect of single-ion zero-field splitting and a weak antiferromagnetic coupling between the M(II) metal centers. Interestingly, due to a severe temperature independent paramagnetic (TIP) contribution, the μ_{RT} values of glasses become high and unevaluable (Fig. S17b).[21]

2.4.2 Spectroscopic study. FT-IR bands at 2278 cm^{-1}, 2163 cm^{-1} (s; ν_{as}(C≡N)) and 1346 cm^{-1} (s; ν_s(C≡N)) slightly red shifted and broadened in the melt-quench glasses (Fig. 4a). Unlike the previous dicyanamide based hybrid organic–inorganic networks,[11] the present glasses reveal the absence of any new band in the FT-IR spectra, indicating no high temperature deformation of the *dca* ligand into a triazine type structure during melt-quenching. In addition, the Raman spectra of crystals and melt-quench glasses exhibit very trivial differences in frequencies, reflecting retainment of the framework structure (Fig. 4b). The weak band at 200 cm^{-1} was linked to M–N bonds or a low-energy electronic motion coupled with vibrations significantly reduced in intensity.

To gain more insight into the chemical nature, we have acid-digested the crystalline and glassy samples and carried out liquid-phase ^{31}P, ^{1}H, and ^{13}C NMR spectroscopy (Fig. 5a–c). Like FT-IR and Raman spectroscopy, in-line observation was noted in the NMR spectra. A ^{31}P signal (23 ppm) assigned to the PrPh$_3$P$^+$ unit was obtained in ^{31}P NMR spectra for both crystals and glasses (Fig. 5a).[21] The ^{1}H spectra (Fig. 5b) show signals for aliphatic moieties at 3.5 ppm (–CH_2–CH_2–CH$_3$), ~1.3 ppm (–CH$_2$–CH_2–CH$_3$) and ~0.7 ppm (–CH$_2$–CH$_2$–CH_3). In all ^{1}H spectra, few overlapping signals assigned to the protons in the phenyl rings are observed at ~7.5 ppm.[21] The presence of a broad signal above ~8.1 ppm seen in some ^{1}H spectra was ascribed to residual H$_3$O$^+$.[1] ^{13}C NMR signals corresponding to the aliphatic and aromatic carbons were clearly visible in all the spectra, whilst the poor signal-to-noise ratio weakens the visibility of dca$^-$ units (Fig. 5c).[21]

2.4.3 Pair-distribution function (PDF) analysis. To explicitly confirm the bonding pattern obtained from spectroscopic data, we have performed the *ex situ*, room-temperature X-ray total scattering experiments on the crystalline and glassy samples. The structure factor, $F(Q)$, extracted after processing

the data show Bragg peaks for crystalline samples whereas the glasses reveal smooth broad humps (Fig. S18). This indicates complete loss of crystallinity after melt-quenching. The pair distribution functions (PDFs, $D(r)$) were extracted after
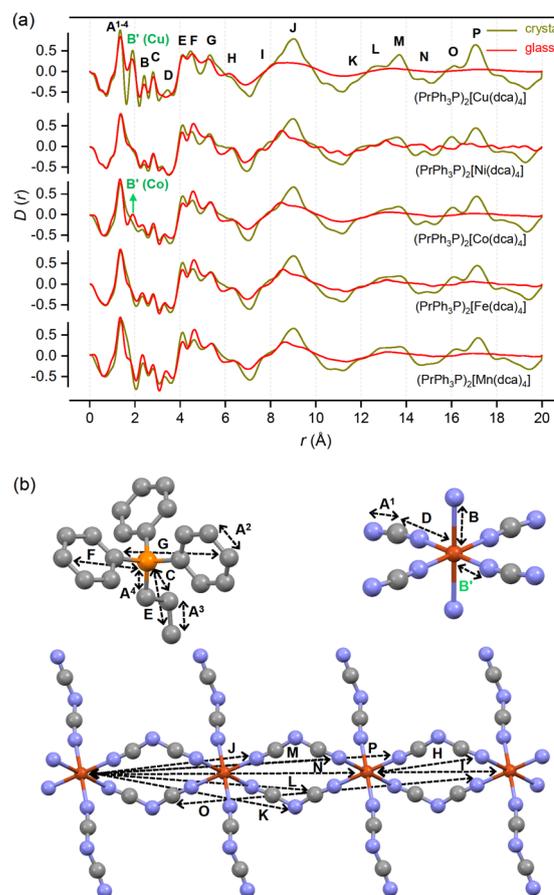

Fig. 6 (a) Pair distribution functions for (dark yellow) (PrPh$_3$P)$_2$[M(dca)$_4$] and (red) a_g(PrPh$_3$P)$_2$[M(dca)$_4$] at room temperature. (b) The A cation and octahedral Cu-dca unit (on top), and extended 1-D Cu-dca network (on bottom) of (PrPh$_3$P)$_2$[Cu(dca)$_4$] at 100 K to identify the peak positions in Fig. (a) (brown: Cu; orange: P; grey: C; blue: N; H atoms omitted for clarity).

appropriate data corrections (Fig. 6a and S19) using experimental pycnometric densities (Table S3). Owing to the similar network connectivity, the PDF peak widths and positions of all the crystalline compounds appear similar up to 20 Å (Fig. S19a). The broad correlation at $\sim r = 1.3–1.8$ Å, contains contributions predominately from C≡N, C=C, C–C, and C–P atom pairs ($\overset{1}{\overleftrightarrow{A}} – \overset{4}{\overleftrightarrow{A}}$, Fig. 6b). The correlation at $r = \sim 2.3$ Å is mainly ascribed to the M–N pair ($\overleftrightarrow{B}$). For $(PrPh_3P)_2[Cu(dca)_4]$, the Cu–N pair shows two peaks at $r = 2.0$ Å and 2.4 Å due to the J–T effect. The peaks at 2.8 Å and 3.4 Å were ascribed to the P⋯C ($\overleftrightarrow{C}$, via the P–C–C linkage) and Mn⋯C ($\overleftrightarrow{D}$, via the Mn–N–C linkage) correlations. Three peaks at 4.1 Å, 4.6 Å and 5.3 Å represent P⋯C ($\overleftrightarrow{E}$), P⋯C ($\overleftrightarrow{F}$) and C⋯C ($\overleftrightarrow{G}$) correlations, respectively. High r correlations at 6.2 Å, 7.6 Å, and 9.0 Å were assigned to Mn⋯N ($\overleftrightarrow{H}$), Mn⋯Mn ($\overleftrightarrow{I}$), and Mn⋯N ($\overleftrightarrow{J}$) respectively. The highest contribution to the peak at $r = 9.0$ Å is largely coming from the M⋯N correlation in every case.

The resemblance in $F(Q)$ and $D(r)$ for all the glasses indicates that they have similar atom–atom correlations in the glassy phase (Fig. S19b). However, the peak centered at around $r = \sim 9.0$ Å was slightly blue shifted and reduced in intensity. This would therefore indicate the twist in chain length as well as retention of maximum M–dca–M linkages. Major correlations above 12.0 Å were mostly vanished which is consistent with the mechanism of melting involving the decoordination–recoordination of Mn–N bonds, and the associated movement of the A site PrPh_3P cations. Still, the retainment of maximum pair correlations up to $r = \sim 12.0$ Å indicate that direct quenching from the $T_{m\text{-offset}}$ leads to less loss in the long-range order alike any other melting MOFs such as ZIFs.[25]

2.5 Mechanical properties

To check the network rigidity upon melt-quenching, we have evaluated the pycnometric density of crystal and glass samples. The melt-quenched glasses appear slightly denser than the crystals, as observed for zeolites and collapsed zeolite structures.[26] This led to a high value of glass-crystal network density deficit, $(\Delta\rho/\rho_g)_{network}$ (Table S3). The mechanical strength of melt-quenched $a_g(PrPh_3P)_2[M(dca)_4]$ glass samples was probed by the nanoindentation method (Fig. S20). The hardness (H) of the glasses evaluated reflects the resistance of the glasses to plastic deformation (Table 1). Values of H ranging between 0.2 and 0.4 ($\pm$0.02) GPa were comparable to those of various MOF based glasses $e.g.$ 0.7 for a_gZIF-62, 0.9 for a_gZIF-4, and 9.73 for Zn-DCl-glass (DCl = 4,5-dicyanoimidazole).[6,27,28] The high H value for $a_g(PrPh_3P)_2[Ni(dca)_4]$ was attributed to its comparatively high T_g.

3 Conclusions

The effect of dimensionality in the solid–liquid phase transition in organic–inorganic hybrid structures has not been observed before. In this study, we have synthesized 1-D hybrid network structures from the perspective of direct vitrification at laboratory time scales and found that lowering the dimensionality plays a critical role in the melt-quenching phenomenon. In the present 1-D networks, the structural configuration exhibits a directional nature owing to its chain like conformation which orients the organic A cations randomly (known as atacticity) at high thermal energy and refuses to reorient then in the ordered fashion after melt-quenching.[19] This suppresses the recrystallization event and results in a perfectly vitrified amorphous state. Large differences in the temperatures between T_d and T_m (>100 °C) also help the viscous state to remain stable well below T_d. The relatively low melting temperatures of the present 1-D hybrid organic−inorganic systems ($T_m \sim 95$ °C for $(PrPh_3P)_2[Cu(dca)_4]$), together with low liquid fragility indices ($m < 50$) and high glass forming ability ($T_g/T_m \sim 0.75$), suggest higher accessibility and processability of the liquid states. Similarly, the large 'glass-crystal network density deficit' was add-on to this.

Another important aspect of the work is melt-quenching under non-inert, cost-effective and less-robust aerobic conditions. Here, melting opens new routes to hybrid glasses by utilizing the structural versatility of the crystalline state. $In\ situ$ glass formation from liquids will prove to be of great interest in producing precise, desired morphologies via other processes such as melt-casting or -spinning. Absence of recrystallization in the melt-quench glasses will give access to the facile growth of thin films and palleted materials, for device fabrication. Maximum retainment of the network structure after melt-quenching led to a denser glass and eventually resulted in a high $(\Delta\rho/\rho_g)_{network}$ and high hardness.[27,29] This can overcome mechanical stress and enhance the lifetime of a material. Using the above versatile properties, we expect that the family of present 1-D hybrid-glasses can be expanded for various applications $e.g.$, in advanced photonics,[30] energy harvesting thermoelectric, $etc.$ in the near future.

4 Materials and methods

4.1 SCXRD

Single-crystal X-ray diffraction (SCXRD) data were collected on a Bruker D8-Venture X-ray diffractometer equipped with an IMS microsource with MoKα radiation ($\lambda = 0.71073$ Å), a Bruker Photon III detector and a Helios optic, using the Bruker APEX4 software.

4.2 PXRD

4.2.1 Ambient temperature. Powder X-ray diffraction (PXRD) patterns of the as-synthesized (as) samples were measured ($2\theta = 5°–60°$) on a Rigaku Benchtop MiniFlex 600-C X-ray diffractometer (Cu Kα radiation, $\lambda = 1.5418$ Å). Data were collected using a 2θ step size of 0.02°, with 10 s per step. Pawley refinement was carried out using TOPAS academic v6 software.[31]

4.2.2 Variable temperature. The experiments were conducted using an Empyrean Panalytical X-ray diffractometer (Cu Kα source, $\lambda = 1.540598$ Å) with a PIXcel detector in 1D scanning mode. The Bragg–Brentano geometry was used with a 10 mm

length-limiting slit and a 2.5° Soller slit at the incident section, a 2.5° Soller slit with a Kβ filter, and a programmable anti-scattering slit in the receiving part. A powder sample (~180 mg) was placed on a corundum holder and installed in an Anton Paar XRK 900 reaction chamber, which was connected to the diffractometer. The heating stage was connected to a chiller where continuous flow of water was maintained to achieve fast cooling. Diffraction patterns were collected with a step size of 0.02° at a rate of 10° min^{-1}.

4.3 Thermal analysis

To determine the temperature of decomposition, thermogravimetric analysis was carried out in an SDT apparatus (TGA STA 449 F5 Jupiter) under an argon atmosphere (note: argon gas was applied for the exact determination of T_d values by avoiding any pre-oxidation process at high temperature). Data were collected in the range from 25 °C to 450 °C at a scan rate of 10 °C min^{-1}. To obtain the temperature of melting (liquid states) using the DSC technique, the samples (~20 mg) were placed in a 70 μL Alumina crucible and heated under aerobic conditions using dry air at their respective melting offsets at a rate of 10 °C min^{-1}. DSC measurements were conducted using a TA Q2000 instrument.

4.4 Preparation of glasses

a_g(PrPh$_3$P)$_2$[M(dca)$_4$]: the (PrPh$_3$P)$_2$[M(dca)$_4$] (M = Mn, Fe, Co, Ni, Cu) single crystals (Fig. 1b, left) were heated under aerobic conditions at 10 °C min^{-1} to ~5 °C above their $T_{m\text{-offset}}$, and then cooled to −50 °C at *ca.* 10 °C min^{-1} to obtain glass samples (Fig. 1b, right).

4.5 Magnetic study

A SQUID MPMS XL instrument was used to conduct magnetic measurements. Details regarding the sample preparation are given in the SI.

4.6 Elemental analysis

The determination of the CHN-values (simultaneously) is based on combustion/GC analysis with a EuroEA Elemental Analyzer (HEKAtech). The error range is ± 0.3%. After acidic digestion and preparation for photometric measurement, phosphorus is determined by absorption at λ = 410 nm (Cary 100 UV/VIS-photometer made by Agilent). The error range is ± 0.5%.

4.7 FT-IR study

Fourier-transform infrared spectra were collected in transmittance mode using a PerkinElmer Frontier™ FT-IR spectrometer on crystal and glass samples.

4.8 Nuclear magnetic resonance (NMR)

Liquid-phase NMR experiments were performed on a 9.4 T Bruker Avance III HD spectrometer equipped with a 5 mm BBFO probe. 8 mg of the sample were digested in 100 μL of 35 wt% DCl in D$_2$O and the mixture was dissolved in 500 μL of DMSO-d_6. Additionally, 50 μL of 85 wt% H$_3$PO$_4$ in H$_2$O were added to reference the ^{31}P spectra. ^{1}H chemical shifts are reported relative to the ^{1}H signal corresponding to the residual protons in DMSO-d_6 at 2.50 ppm,[21] while ^{31}P and ^{13}C chemical shifts are referenced to the ^{31}P H$_3$PO$_4$ signal at 0.00 ppm and the ^{13}C DMSO-d_6 signal at 39.50 ppm,[32] respectively. ^{31}P and ^{13}C experiments were performed with ^{1}H decoupling. ^{1}H, ^{31}P and ^{13}C spectra were recorded with 196, 600 and 3840 scans, respectively.

4.9 X-ray total scattering experiments

Room temperature measurements were performed on a sample of crystalline and melt-quenched glass separately. Data were collected at the I15-1 beamline at the Diamond Light Source, UK (λ = 0.158345 Å, 78.3 keV) in the range of 0.6 < Q < 24 Å^{-1}. Finely ground samples of the crystals and glasses were loaded into 1-mm-diameter borosilicate glass capillaries and capped with glue to keep the powder in place during the data collection. Data on the empty instrument and capillary were also collected in the same region of 0.6 < Q < 24 Å^{-1}. Background, multiple scattering, container scattering, Compton scattering, and absorption corrections were performed using the GudrunX program.[33]

4.10 Network density measurements

Physical densities of all crystals and glasses were measured using a Micromeritics Accupyc 1340 helium pycnometer. The typical mass used for each test was around 80 mg. The reported values were averaged over a cycle of 3 measurements.

4.11 Nanoindentation

The specimens were embedded in epoxy resin and subsequently polished to a mirror finish in preparation for instrumented indentation testing. Measurements were conducted using a NanoTest Vantage system (Micro Materials Ltd., UK) in accordance with DIN EN ISO 14577. A constant indentation depth of 1000 nm was maintained, with the required loads varying depending on the material response. Indentation was performed using a three-sided Berkovich diamond indenter, pre-calibrated with fused silica as the reference material. Poisson's ratio was set to ν = 0.2, following established values in the literature. Hardness values were subsequently derived from the load–displacement data and verified through optical scans of the individual indentations.

Author contributions

S. K. & B. K. S. designed the project and wrote the manuscript with input from all authors. S. K. and B. K. S. synthesized the materials. B. K. S. and P. S. collected the VT-PXRD data and S. K. analyzed the data. S. A. H. collected the SCXRD data and S. K. & B. K. S. analyzed the data. B. K. S. collected the PXRD, TG, DSC, FT-IR, elemental, magnetic, and nanoindentation data and S. K. analyzed the data. B. K. S. processed and analyzed the X-ray total scattering data, collected at the I15-1 beamline, Diamond Light Source.

Conflicts of interest

There are no conflicts to declare.

Data availability

Acknowledgements

Notes and references

1 B. K. Shaw, A. R. Hughes, M. Ducamp, S. Moss, A. Debnath, A. Sapnik, M. Thorne, L. N. McHugh, A. Pugliese, D. Keeble, P. Chater, J. Bermudez-Garcia, X. Moya, S. K. Saha, D. Keen, F.-X. Coudert, F. Blanc and T. D. Bennett, *Nat. Chem.*, 2021, **13**, 778–785.

2 K. Tanaka, Y. Tago, M. Kondo, Y. Watanabe, K. Nishio, T. Hitosugi and M. Moriya, *Nano Lett.*, 2020, **20**, 8200–8204.

3 M. Dai, B. Zhou and D. Yan, *Angew. Chem., Int. Ed.*, 2025, **64**, e202505322.

4 F. Nie and D. Yan, *Acc. Chem. Res.*, 2025, **58**, 3010–3020.

5 B. Zhou and D. Yan, *Matter*, 2024, **7**, 1950–1976.

6 F. Nie, K.-Z. Wang and D. Yan, *Nat. Commun.*, 2023, **14**, 1654.

7 D. Umeyama, S. Horike, M. Inukai, T. Itakura and S. Kitagawa, *J. Am. Chem. Soc.*, 2015, **137**, 864–870.

8 B. Li, Y. Wang, Y. Xu and Z. Xia, *Adv. Mater.*, 2025, **37**, 2415483.

9 F. Nie and D. Yan, *Nat. Commun.*, 2024, **15**, 5519.

10 Y. Rong, A. M. Chester, B. Turner, G. P. Robertson, A. Kono, P. A. Chater, L. N. McHugh, D. A. Keen, T. D. Bennett and C. Castillo-Blas, *Chem. Commun.*, 2025, **61**, 12566–12569.

11 B. K. Shaw, C. Castillo-Blas, M. F. Thorne, M. L. Ríos Gómez, T. Forrest, M. D. Lopez, P. A. Chater, L. N. McHugh, D. A. Keen and T. D. Bennett, *Chem. Sci.*, 2022, **13**, 2033–2042.

12 L. Frentzel-Beyme, M. Kloß, R. Pallach, S. Salamon, H. Moldenhauer, J. Landers, H. Wende, J. Debus and S. Henke, *J. Mater. Chem. A*, 2019, **7**, 985–990.

13 M. Liu, R. D. McGillicuddy, H. Vuong, S. Tao, A. H. Slavney, M. I. Gonzalez, S. J. L. Billinge and J. A. Mason, *J. Am. Chem. Soc.*, 2021, **143**, 2801–2811.

14 A. Singh, M. K. Jana and D. B. Mitzi, *Adv. Mater.*, 2021, **33**, 2005868.

15 A. Singh, Y. Kim, R. Henry, H. Ade and D. B. Mitzi, *J. Am. Chem. Soc.*, 2023, **145**, 18623–18633.

16 C. A. Angell, *Science*, 1995, **267**, 1924–1935.

17 G. N. Greaves and S. Sen, *Adv. Phys.*, 2007, **56**, 1–166.

18 L. M. Wang, C. A. Angell and R. Richert, *J. Chem. Phys.*, 2006, **125**, 074505.

19 U. Ali, K. Karim and N. Buang, *Polym. Rev.*, 2015, **55**, 678–705.

20 E. D. Zanotto and D. R. Cassar, *Sci. Rep.*, 2017, **7**, 43022.

21 B. K. Shaw, L. Corti, J. M. Tuffnell, C. Castillo-Blas, P. Schlachta, G. P. Robertson, L. McHugh, A. F. Sapnik, S. A. Hallweger, P. A. Chater, G. Kieslich, D. A. Keen, S. E. Dutton, F. Blanc and T. D. Bennett, *Inorg. Chem.*, 2024, **63**, 24812–24824.

22 N. Ma and S. Horike, *Chem. Rev.*, 2022, **122**, 4163–4203.

23 R. Gaillac, P. Pullumbi, K. A. Beyer, K. W. Chapman, D. A. Keen, T. D. Bennett and F.-X. Coudert, *Nat. Mater.*, 2017, **16**, 1149–1154.

24 A. Qiao, T. D. Bennett, H. Tao, A. Krajnc, G. Mali, C. M. Doherty, A. W. Thornton, J. C. Mauro, G. N. Greaves and Y. Yue, *Sci. Adv.*, 2018, **4**, eaao6827.

25 S. Horike, S. S. Nagarkar, T. Ogawa and S. Kitagawa, *Angew. Chem., Int. Ed.*, 2020, **59**, 6652–6664.

26 G. N. Greaves, F. Meneau, A. Sapelkin, L. M. Colyer, I. ap Gwynn, S. Wade and G. Sankar, *Nat. Mater.*, 2003, **2**, 622–629.

27 T. D. Bennett, Y. Yue, P. Li, A. Qiao, H. Tao, N. G. Greaves, T. Richards, G. I. Lampronti, S. A. T. Redfern, F. Blanc, O. K. Farha, J. T. Hupp, A. K. Cheetham and D. A. Keen, *J. Am. Chem. Soc.*, 2016, **138**, 3484–3492.

28 B. Zhou, Z. Qi and D. Yan, *Angew. Chem., Int. Ed.*, 2022, **61**, e202208735.

29 R. K. Guntu, V. Venkatramu, Ch. S. Rao and V. R. Kumar, *Opt. Mater.*, 2021, **113**, 110876.

30 R. K. Guntu, in *Bioresorbable Polymers and their Composites*, 2024, pp 421–442.

31 A. A. Coelho, *J. Appl. Crystallogr.*, 2018, **51**, 210–218.

32 H. E. Gottlieb, V. Kotlyar and A. Nudelman, *J. Org. Chem.*, 1997, **62**, 7512–7515.

33 A. K. Soper, *GudrunN and GudrunX: Programs for Correcting Raw Neutron and X-Ray Diffraction Data to Differential Scattering Cross Section*. Tech. Rep. RAL-TR-2011-013, 2011.

34 (*a*) CCDC 2480284: Experimental Crystal Structure Determination, 2026, DOI: 10.5517/ccdc.csd.cc2p7y52; (*b*) CCDC 2480285: Experimental Crystal Structure Determination, 2026, DOI: 10.5517/ccdc.csd.cc2p7y63; (*c*) CCDC 2480286: Experimental Crystal Structure Determination, 2026, DOI: 10.5517/ccdc.csd.cc2p7y74; (*d*) CCDC 2480287: Experimental Crystal Structure Determination, 2026, DOI: 10.5517/ccdc.csd.cc2p7y85; (*e*) CCDC 2480288: Experimental Crystal Structure Determination, 2026, DOI: 10.5517/ccdc.csd.cc2p7y96.